Materials & Design 210 (2021) 110072

Contents lists available at ScienceDirect

Materials & Design

journal homepage: www.elsevier.com/locate/matdes

Achieving homogeneity in a high-Fe β-Ti alloy laser-printed from blended elemental powders

Farheen F. Ahmed [a], Samuel J. Clark [b,c], Chu Lun Alex Leung [b,g], Leigh Stanger [d], Jon Willmott [d], Sebastian Marussi [b], Veijo Honkimaki [e], Noel Haynes [f], Hatem S. Zurob [a], P.D. Lee [b,g,*], A.B. Phillion [a,*]

[a] Department of Materials Science and Engineering, McMaster University, Hamilton L8S 4L8, Canada
[b] Mechanical Engineering, University College London, London, England WC1E 7J3, United Kingdom
[c] X-ray Science Division, Advanced Photon Source, Argonne National Laboratory, Lemont, IL 60439, USA
[d] Department of Electronic and Electrical Engineering, University of Sheffield, Sheffield, England S1 3JD, United Kingdom
[e] European Synchrotron Radiation Facility, 38000 Grenoble, France
[f] Collins Aerospace, 1400 South Service Road West, Oakville L6L 5Y7, Canada
[g] Research Complex at Harwell, RAL, Didcot OX11 0FA, United Kingdom

HIGHLIGHTS

- In-situ alloying of a Ti-1Al-8V-5Fe powder during Selective Laser Melting was investigated using synchrotron X-ray diffraction and infra-red thermal imaging.
- The alloying process of a β-Ti powder was studied by X-ray diffraction and IR imaging.
- Exothermic mixing aids in melting but this gives a mix of alloyed & unalloyed regions
- A consistent microstructure is only achieved via thermal cycling in the HAZ

GRAPHICAL ABSTRACT

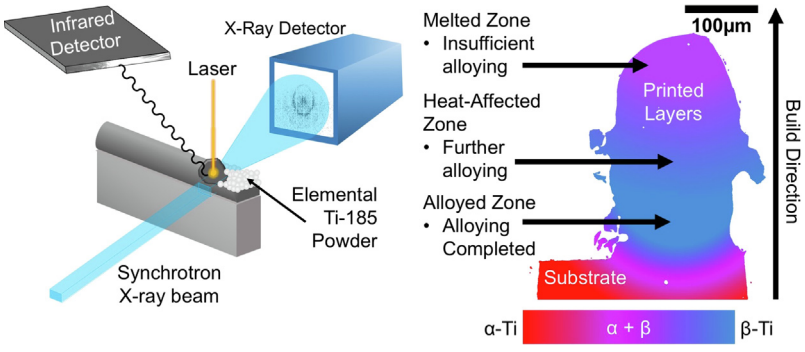

ARTICLE INFO

Article history:
Received 17 June 2021
Revised 13 August 2021
Accepted 24 August 2021
Available online 25 August 2021

ABSTRACT

Blended Elemental powders are an emerging alternative to pre-alloyed powders in metal additive manufacturing due to the wider range of alloys producible with them and the cost savings from not developing novel feedstock. In this study, *in situ* alloying and concurrent microstructure evolution during SLM are investigated by performing SLM on a BE Ti-185 powder while tracking the surface temperatures via Infrared imaging and phase transforma- tion via synchrotron X-ray Diffraction. We then performed post-mortem electron microscopy (Backscatter Electron imaging, Energy Dispersive X-ray Spectroscopy and Electron Backscatter Diffraction) to further gain insight into microstructure development. We show that although exothermic mixing aids the melting process, laser melting results only in a mixture of alloyed and unmixed regions. Full alloying and thus a consistent microstructure is only achieved through further thermal cycling in the heat-affected zone.

© 2021 The Author(s). Published by Elsevier Ltd. This is an open access article under the CC BY license (http://creativecommons.org/licenses/by/4.0/).

1. Introduction

Additive Manufacturing (AM) has grown over the last decade as a class of methods to make near-net-shape parts without significant post-processing, making it a novel alternative to conventional manufacturing processes [1]. AM via Selective Laser Melting (SLM),

* Corresponding authors at: Mechanical Engineering, University College London, London, England WC1E 7J3, United Kingdom (P.D. Lee). Materials Science and Engineering, McMaster University, Hamilton, Canada, L8S 4L7 (A.B. Phillion)

E-mail addresses: peter.lee@ucl.ac.uk (P.D. Lee), andre.phillion@mcmaster.ca (A.B. Phillion).

https://doi.org/10.1016/j.matdes.2021.110072
0264-1275/© 2021 The Author(s). Published by Elsevier Ltd.
This is an open access article under the CC BY license (http://creativecommons.org/licenses/by/4.0/).

which involves repeatedly depositing layers of feedstock powder onto a bed and fusing selected regions with a microscopically-focused laser beam, has particularly grown as a metal AM process [2]. One of its strengths is an ability to create components with novel microstructures that cannot be achieved during conventional processing, as a result of the extremely high cooling rates on the order of $10^5 - 10^6$ K/s [3].

During SLM, alloys are normally printed from pre-alloyed powders (i.e. Ti-6Al-4V powder to build a Ti-6Al-4V part). This limits printing to alloys having commercially available feedstock. However, new alloy compositions that take advantage of the highly non-equilibrium nature of SLM are required to exploit the full potential of this fabrication method [1]. The costs of developing novel feedstock can be mitigated via *in situ* alloying *[2]*. This emerging technique uses pure elemental powders, instead of pre-alloyed ones, that are blended prior to SLM. The Blended Elemental (BE) powder then alloys during melting and in subsequent reheating cycles. Customizability of the alloy composition is greatly expanded, and components with a gradient in composition can also be developed *[4]*. As shown by Dobbelstein *[5]*, the process of alloying requires multiple heating cycles. The initial printing sinters and weakly alloys the powder; complete alloying and homogenization only occurs with the additional heat input that is a result of printing additional layers.

Whether the bulk microstructure completely alloys depends on two main factors: (1) the difference in melting temperature between elements since high melting point particles may not melt thus reducing the bulk alloy composition [6–19]; and (2) the input energy density since high energy densities facilitate mixing over low energy densities [6–8,15,18,20,21,11,12,22,23]. Although all elements will melt and then mix with a high input energy density, using a too-high energy density may vaporize low boiling-point elements and/or cause keyholing [19,22,18,24,23,21].

To understand how to improve the *in situ* alloying process when using BE powder, it is imperative to understand how an alloyed microstructure develops. Few studies have directly examined microstructure development during AM via BE. In one study, Yan et al. *[25]* investigated in situ alloying of BE Ti-6Al-4V during SLM of a thin wall, and observed a decrease in Al and V concentration towards the final layer. Although they attributed this difference in concentration to lesser heat transfer in the single wall than the substrate, a clear discussion of the process of homogenization was not provided. In another, Kang et al. noticed more unmelted Mo near the top than near the bottom of SLM-processed single wall fabricated with BE Ti and Mo powder. Thus, a higher amount of β-phase (stabilized by Mo) was found at the bottom, indicating successful alloying via intrinsic heating cycles. However, they too only offered a limited discussion of microstructural evolution in the partially-alloyed layers *[26]*.

β-Ti alloys are an important class of Ti alloys that are finding increased usage in the commercial aerospace industry owing to their higher tensile and fatigue strengths and increased formability over α-Ti (HCP) and $\alpha + \beta$ alloys [27]. However, they are quite expensive due to a high Mo content. Ti-185 is a low-cost β (BCC)-Ti alloy containing 1Al, 8V, and 5Fe (wt.%) that is being explored [28] for AM applications. In this study, *in situ* alloying and concurrent microstructure evolution during SLM are investigated by performing SLM on a BE Ti-185 powder while tracking the surface temperatures via Infra-red (IR) imaging and phase transformation via synchrotron X-ray Diffraction (sXRD). While sXRD has been previously used to observe phase transformations during SLM *[29–34]*, this is the first study on BE powder and thus of the *in situ* alloying process.

2. Methods

Fig. 1 provides a schematic of the experimental setup whereby SLM, IR imaging, and sXRD were performed concurrently to observe phase transformations *in situ* within the BE Ti-185 powder. The global coordinate system is also indicated: x is the direction of the laser pass; y is the path of the X-ray beam; and z is the vertical (depth) direction. The experiment was performed on Beamline ID-31 of the European Synchrotron Radiation Facility in Grenoble, France. Each stage of the process is described below, along with the method used to obtain the below-surface temperatures as well as details of the post-build microscopy.

2.1. Material

The Ti-185 BE powder consisted of pure Ti (T_m = 1941 K), pure Fe (T_m = 1811 K), and alloyed AlV (T_m = 2093 K [35], approx. 85%V by weight) particles. The mixture was supplied by ADMA Advanced Materials Products, Inc. (Hudson, OH), and had a size distribution with $d_{10\%}$ = 21 μm, $d_{50\%}$ = 51 μm and $d_{90\%}$ = 68 μm, an apparent density of 3.1 g/cm^3, and an oxygen content of 150 ppm. The Al (T_m = 934 K) and V (T_m = 2183 K) were alloyed together to prevent excessive vaporization of Al [18,9]. Due to mixing via ball milling, the powder particles were irregularly shaped [28]. The critical temperatures for this alloy (β_{tr} = 970 K, T_{sol} = 1703 K and T_{liq} = 1849 K) were determined via ThermoCalc^{TM} using the TCTI2 database. This database was also used to determine the Ti-185 thermophysical properties as well as the mixing enthalpies of Ti-185 as well as the binary Ti-1.1 Al, Ti-8.5V and Ti-5.5Fe with respect to their constituent elements. Note that the binary compositions represent the compositions assuming the other elements were excluded.

2.2. Selective Laser Melting

SLM was performed using a bespoke apparatus known as the In Situ and Operando Process Replicator (ISOPR) shown in Fig. 1 [36–39] that utilizes a continuous-wave (1070 nm) laser to fuse powder

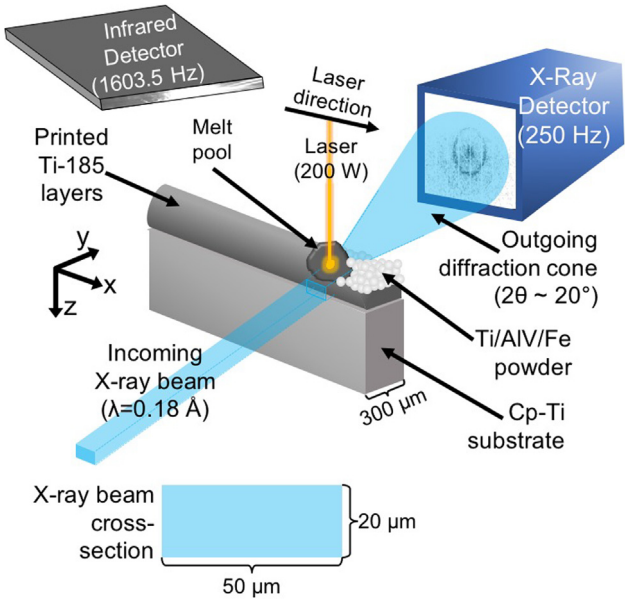

Fig. 1. Setup of real-time sXRD and IR imaging in the ISOPR. Note that this diagram is not to scale to emphasize the different features in the setup.

to a substrate. To contain the powder, the substrate is sandwiched between two panels of glassy carbon, each 300 μm thick and transparent to X-rays. After each pass of the laser, the platform holding the substrate is shifted downwards 25 μm, and then a small vibration-assisted hopper deposits an additional layer from a powder resevoir. In this way, the ISOPR creates thin wall components via single track, multi-layer SLM.

The experiment consisted of printing a 14-layer BE Ti-185 thin wall, 3 cm in length, 100 μm in thickness and 350 μm in height, onto a commercially pure Ti substrate 4.5 cm in length, 300 μm in thickness, and 1.75 cm in height. Printing was conducted in a high-purity Ar environment. The laser energy and travel speed during each single-track pass were 200 W and 400 mm/s. This amounted to an energy density of 66.7 J/mm^3 [40]. Layers 1–5 were initial layers, built to avoid substrate effects when collecting sXRD patterns. Layers 6–10 were used to examine melt crystallization. Layers 11–14 were used to collect sXRD of a single layer (Layer 11) as it underwent multiple reheating cycles during the building of subsequent layers.

2.3. Synchrotron X-ray diffraction

Diffraction images were collected on ID-31 at ESRF using a Dectris Pilatus CdTe 2 M detector placed at 639.6 mm away from the substrate. The λ = 0.1812 Å X-ray beam used for diffraction was rectangular in shape, 50 × 20 μm in cross-section. The detector had a pixel size of 172 μm, a field of view of 253.7 × 288.8 mm, and acquired datasets at 250 Hz with an exposure time of 0.3 ms. The acquired diffraction images were radially integrated to 1D patterns using a Matlab package developed at ESRF [41], and compared to reference patterns of individual phases. sXRD images were not collected for Layers 1–5. While printing Layers 6–10, the sXRD X-ray beam was placed at a target position of 40 μm below the surface. Although this appears to place the X-ray beam in the layer just beneath the powder layer, assuming a 25 μm layer thickness to match the downward motion of the platform, prior experience identified this location as being optimally-aligned with the melt pool. Specifically, layer shrink occurred during printing due to the low bulk density of the BE Ti-185 powder and the occurrence of powder denudation during SLM. For Layers 11 to 14, the ISOPR was shifted upwards by 25 μm between laser passes to track a single layer as it underwent multiple reheating cycles. This displacement is coincident with the platform shift between laser passes.

2.4. IR Imaging

IR imaging (Hamamatsu ORCA-Flash4.0 V3 Digital CMOS camera with a pixel size of 6.3 μm) was performed to measure the surface temperature during each laser pass. A field of view of 2048 x 128 pixels, or 13.312 x 0.832 mm, centred on the printed layer, collected images at a rate of 1603.5 Hz. Individual frames were then translated such that the laser was assumed to be a moving frame of reference travelling at steady-state. Due to shadowing caused by the glassy carbon panels, temperature measurement was limited to the central ± 100 μm in the thickness direction. Although the IR detector operated at temperatures above 958 K, the signal-to-noise ratio was found to be too high at temperatures below 1273 K. As such, this was set to be the minimum-observable temperature.

2.5. Prediction of Below-surface Temperatures

The IR imaging provides only the surface temperature during SLM. Thus, the thin wall [42] form of the Rosenthal equation [43] (Eqs. 1,2), was employed to estimate the below-surface temperatures within the substrate, thin wall, and powder between the two glassy carbon panels,

$$T = \frac{\alpha Q}{\pi k b} e^{-\bar{x_0}} \left(\sqrt{\bar{x_0}^2 + \bar{z_0}^2}\right) + T_0 \text{with} \quad (1)$$

$$\bar{x_0} = \frac{x_0 \rho c V}{2k} \text{and} \bar{z_0} = \frac{z_0 \rho c V}{2k}, \quad (2)$$

where T represents the temperature at coordinates x_0 and z_0 in the scanning and depth directions with respect to the moving laser, T_0 is the ambient temperature, Q is the laser power, α is the absorptivity, k is the thermal conductivity, b is the width of the thin wall, ρ is the density, c is the specific heat capacity and V is the laser scan speed.

The Rosenthal solution assumes that material properties are constant, the laser is a point heat source, heat is lost only through conduction via the layers below and/or the substrate, and radiation and convection to the surroundings are negligible [42]. Owing to these assumptions, only temperatures below the solidus can be predicted with any accuracy since at fluid convection at temperatures above the solidus significantly accelerates heat transfer far beyond the limit for constant material properties.

The material properties for Ti-185 (ρ = 4558 kg/m^3, k = 25 W/m·K, C_p= 723 J/kg·K) at 1703 K, corresponding to the solidus temperature for this alloy, were used for the calculation. The properties at the solidus were selected to best reflect the thermal behaviour at high temperatures.

2.6. Microscopy

Scanning Electron Microscopy (SEM) was performed at the Canadian Centre for Electron Microscopy in Hamilton, Canada on the SLM-printed single-track Ti-185 thin wall. Specifically, Backscatter Electron (BSE) and Energy Dispersive Spectroscopy (EDX) were performed using a JEOL 6610 LV, and Electron Backscatter Diffraction (EBSD) was performed using a JEOL 7000. Prior to SEM, the sample was sectioned into three 1-cm-long segments along the scanning direction to preserve the melted and heat-affected zones for analysis, followed by mounting in epoxy. Grinding (SiC paper with 600, 800, and 1200 grit) and polishing (diamond 3 μm suspension followed by colloidal silica 1 μm and 20% hydrogen peroxide) were performed with an automatic polisher on co-rotation. Finally, each section was coated with carbon and with Ni paint.

3. Results

3.1. Overview of the SLM process

Fig. 2 shows a schematic of the build's cross-section after printing a) Layer 1, b) Layer 6, c) Layer 10 and d) Layer 14. The position of Layer 1 is indicated in b), c) and d) to show the downward motion of the platform. Beginning with a) it can be seen that while the substrate is nicely contained between the glassy carbon, not all the powder fuses because the laser spot size was thinner than the substrate width. Thus, α-Ti, AlV and Fe powder remain after printing. As the layers continue to build (images b,c), the amount of unmelted powder is seen to increase.

3.2. X-ray diffraction during SLM

Fig. 3 shows the sXRD peak evolution for the phase transformations at the melt pool surface, acquired during the printing of Layer 6. XRD patterns are shown before printing (0 ms), at the start of the phase transformation (4 ms) and at its completion (36 ms). Upon laser heating, the powder melted, however because it was molten

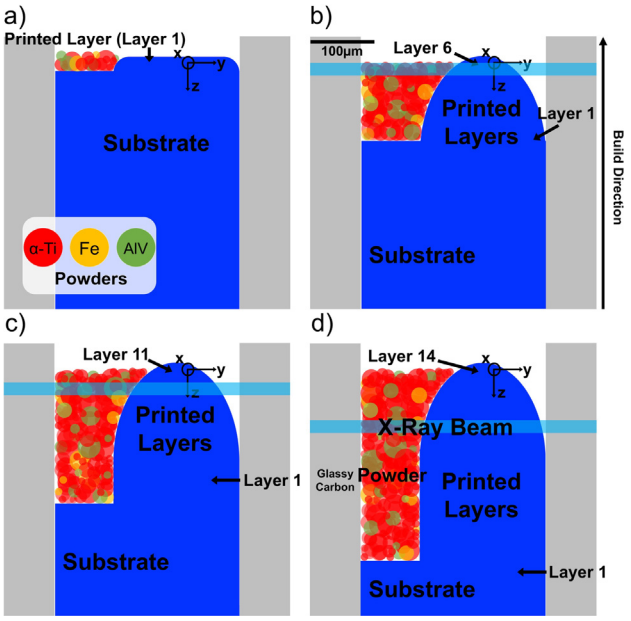

Fig. 2. Schematic of the single-track, multi-layer printing process after SLM of a) Layer 1, b) Layer 6, c) Layer 11 and d) Layer 14 in cross-section view (the laser path is "into the page"). The Ti substrate and printed layers are shown in blue; the glassy carbon plates are grey, and the un-melted powder is red, yellow, and green. The X-ray beam position is also shown for reference in b), c) and d) (data was not acquired for layers 1–5). To interpret the colour in this figure, please refer to the web version of this paper.

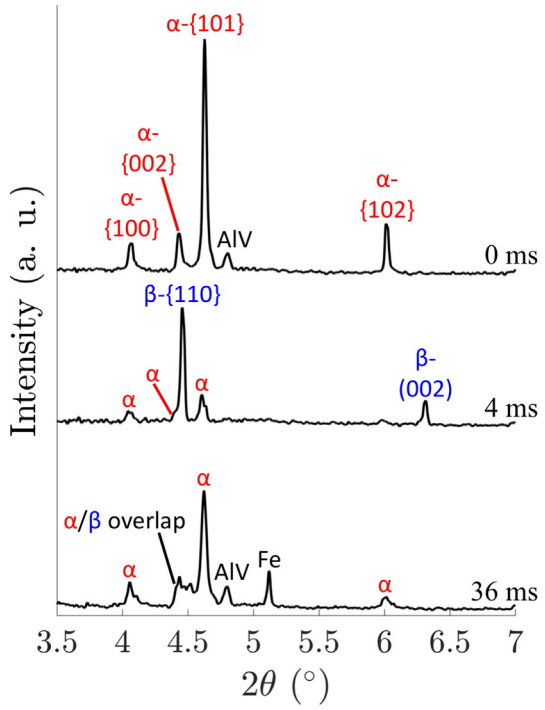

Fig. 3. sXRD data collected for Layer 6. Frames are shown before printing (0 ms), at the start of the phase transformation (4 ms) and at its completion (36 ms).

for only ~1.5 ms (see Fig. 7), an amorphous melt curve was not observed in the image collected at 4 ms; as the acquisition rate was 250 Hz, intermediate images could not be collected. Note that as the beam size is small the grain statistics are insufficient to perform quantitative sXRD. However, as can be seen, there are sufficient grains to produce a signal that allows for phase identification. Note also that the missing AlV and Fe peaks is a result that powder moves in and out of the sampling volume due to Marangoni flow effects and spatter.

The first signs of a phase transformation were the suddenly-high β-Ti and low α-Ti signals (middle line, Fig. 3). Over the course of the phase transformation, the β-peaks are seen to shift towards higher angles i.e. decreasing the lattice parameter. This is because of a combination of sample cooling, and an increase in amount of Fe and V dissolved in the β phase. The β intensities also decreased, while α intensities increased up until the end of the phase transformation. The phase transformation ended at approximately 36 ms. At the end of the phase transformation period, a weak β-{110} peak was seen to overlap with the α-{002} peak. Alone, this would suggest that a low amount of β was retained. However, the α signals are also quite low. This, along with the fact that there were considerable unmelted powders, as discussed below, meant that much of this α-Ti was likely not part of the printed layer. Thus the presence of β is inferred.

The presence of unmelted particles, shown in Fig. 2, made interpretation of the sXRD images difficult. Despite not being part of the printed sample, these unmelted particles still diffracted the incoming X-rays and thus produced a signal that was collected by the detector. Because of heat conduction, the unmelted pure α-Ti powders would have transformed to β during SLM, but upon cooling they would have immediately reverted to α [27]. Hence, they would have provided an additional α-Ti signal both before and after heating, and additional β-Ti signal while the temperature was greater than the β-transus. As the exact temperature for each frame was unknown, some frames had both additional α-Ti and β-Ti over-and-above the signal collected from the Ti-185 melt pool.

Melt-pool diffraction data was collected for each of Layers 6–10. In general, the results were similar with all containing α-Ti peaks. However, only some contained weak AlV or Fe peaks, and one did not show any of these peaks. The starting intensities of the peaks, at 0 ms, also varied between the five repeats. The observed variations are due to a combination of the size of the acquisition volume and the random sampling of powders. The variability in phase transformation end time was 36 ± 14 ms. Further, only one showed a distinct β-{002} peak after the laser beam had passed.

Fig. 4 a) shows the post-phase transformation sXRD patterns collected for Layer 11 as it underwent multiple melting and reheating cycles due to the printing of Layers 11–14. This corresponds to depths of 40, 65, 90, 115 and 140 μm below the build surface.

At 65 μm below the surface, Fig. 4 a) shows that the sample heated up to a mixture of high β and low α intensities. As compared to the pre-reheating frame, the β peaks were seen to shrink and shift to the right with respect to the initial phase transformation peaks during cooling. However, they did not fully disappear, coexisting along the with the α peaks. At 90 μm below the melt pool, this combination was reheated to both high β and low α peaks. The β peaks again shrank and shifted to the right, while the α peaks re-emerged, without fully disappearing. The same process occurred at 115 and 140 μm below the surface. Note that due to the accumulation of unmelted powders, it is possible that this sample had less α-Ti than was indicated in the plots.

Fig. 4 b) shows the post-phase transformation sXRD peaks at depths of 115 and 140 μm below the surface, with the intensity magnified by a factor of 13.3. These images directly show the presence of the β-{002} peak, further demonstrating that the overlapping α-{002}/β-{110} were predominantly β-{110} at these depths.

Traditionally, Rietveld refinement used to analyze sXRD peak intensity and locations. Unfortunately, it was not possible to apply this technique on the collected data. This is for a number of reasons: (i) the sample temperature is not uniform; (ii) the exact composition of Ti in the melt pool is unknown, and therefore the appropriate equilibrium lattice parameters for each temperature

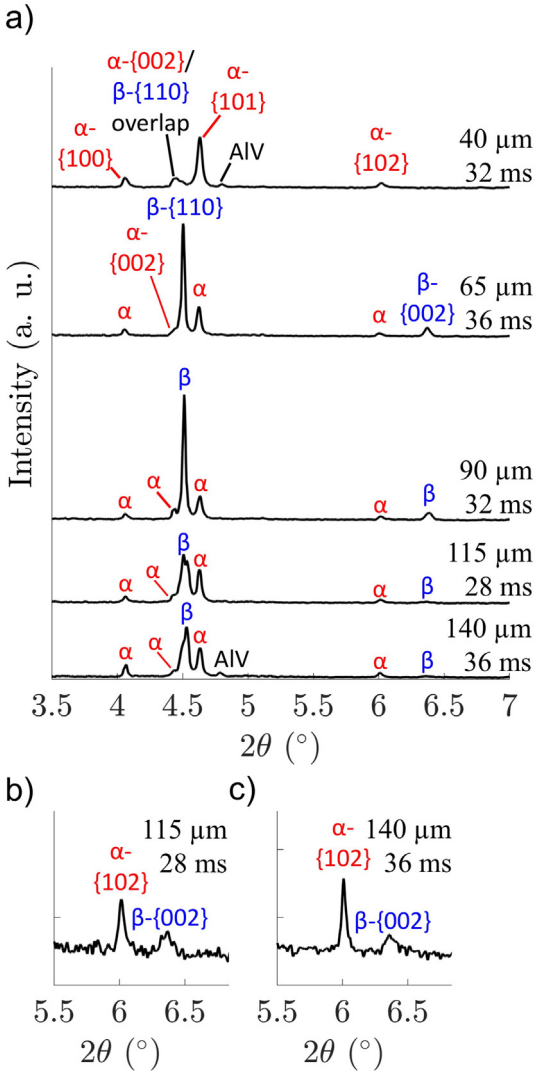

Fig. 4. a) Post-phase-transformation sXRD frames after each laser pass when a single layer was tracked through reheating cycles. The duration of each phase transformation is also shown. b) and c) show the α{102} and β-{002} peaks in the $2\theta = 5.5–6.7°$ range with the intensity magnified by a factor of 13.3 at depths of 115 and 140 µm respectively.

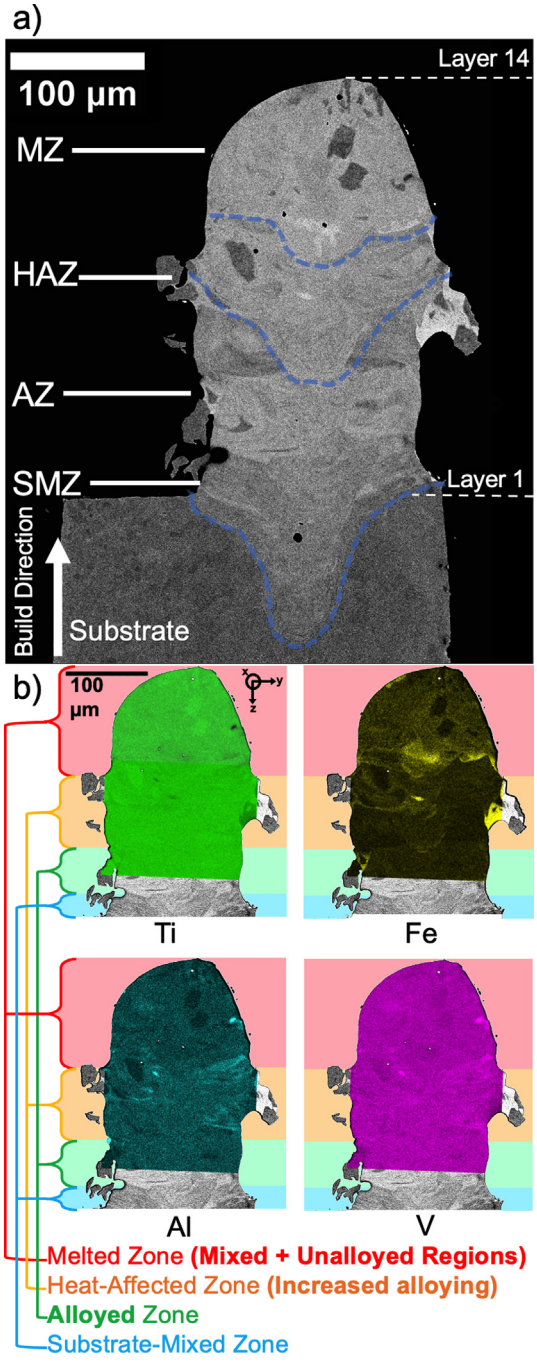

Fig. 5. a) BSE image of the printed layers cross-sectioned perpendicular to the scanning direction. Example melt pool boundaries showing keyholing are highlighted in blue. b) EDX maps of Ti, Fe, Al and V; MZ = Melted Zone, HAZ = Heat Affected Zone, AZ = Alloyed Zone, SMZ = Substrate Mixed Zone. To interpret the colour in b), the reader is referred to the web version of this paper.

are unknown; (iii) the rapid cooling results in a non-equilibrium lattice parameter due to the buildup of internal stresses; (iv) the IR imaging data and Rosenthal equation (discussed below) provide an estimation of temperature only without enough accuracy to carry out Reitveld analysis.

3.3. Microscopy

SEM, EDX, and EBSD were conducted on the SLM-printed sample.

Fig. 5 a) shows an SEM (BSE) image of the Ti-185 thin wall cross-section (perpendicular to the scanning direction). A number of salient observations can be made. First, the cross-section varies between the centreline and edges of the sample, as heat was most concentrated at the centreline. Hence, the degree of alloying was investigated with reference to the centreline and not the edges. As can be seen, the depth of the melted zone and heat-affected zone are clearly evident. The melt pool is ≈100 µm deep at the edges, but 140 µm at the centre. The heat-affected zone extends up to 230 µm deep. At this point, the microstructure is consistent until 300 µm, suggesting that it is alloyed. At 300 µm, the substrate-mixed zone begins. This zone continues up until 400 µm, at which point the sample appears to be completely substrate. Second, lines indicating the visible melt pool contours - having keyhole shape - that formed during the printing process. These lines appear because of the single-track SLM; in an actual printed microstructure, the edges will be heated due to the printing of multiple hatches. Third, the thin wall has a thickness of ≈ 200 µm, leaving a 100-µm thick gap in which unmelted powders accumulated, confirming that sXRD detected more α-Ti than was present in the printed sample.

Fig. 5 b) shows the corresponding EDX images for each alloying element. As can be seen, the melted zone alternates between evenly-alloyed regions and those concentrated in a single element (or two, in the case of Al and V). In the heat-affected zone, there is less homogeneity near the edges due to a lower heat input there. However, near the centre of each layer, the sample increases in homogeneity down the build direction. The sample is homogenous in the alloyed zone. Note that high-resolution EDX images of the Melted Zone and Heat Affected Zone are provided as supplemental images S1-S4.

Fig. 6 shows the corresponding EBSD image of the printed layers with a) and b) being the orientation map and the phase map of the whole section, c) and d) being the orientation map and phase map of a section within the melt pool, and e) indicating the colour coding for the phase maps in a) and c). In Fig. 6 a) and b), the boundary between the melted zone and the heat-affected zone is not clear. However, for the purposes of interpretation we can use the mushy zone depth determined from BSE imaging (Fig. 5 a)) of $\sim$ 100 µm at the edges and 140 µm at the centre. The boundary between the heat-affected zone and the rest of the sample is clear. Specifically, this boundary is where there are no longer large (10–40 µm wide), curved regions of α, and only small regions of α remain. This zone extends up to the substrate-mixed zone. In the melted zone, a mixed $\alpha + \beta$ structure is observed with some layers having more than 50% α. The heat-affected zone is mostly β. However, some α is present as curved regions 10–40 µm wide. Within the heat-affected zone, the larger regions of α formed along the melt pool boundaries. Below the heat-affected zone, α is present in the form of small regions <3 µm in size (approximately 1–2 pixels wide) at the grain boundaries.

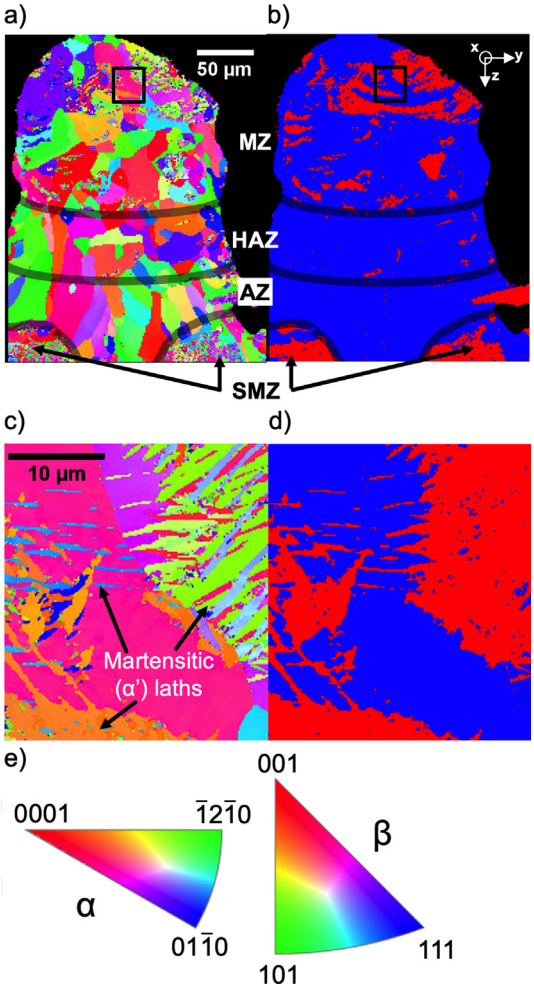

Fig. 6. a) Orientation map and b) Phase map of the entire printed layer; c) Orientation map and d) Phase map of a high-resolution image of the melted zone area highlighted in a) and b); and e) Legend for orientation maps a) and c). In b) and d), the α and β are represented by red and blue respectively. Grain orientations are with respect to the build direction (vertical, pointing upwards). The scanning direction is into the page. To interpret the colour in this figure, the reader is referred to the web version of this paper; MZ = Melted Zone, HAZ = Heat Affected Zone, AZ = Alloyed Zone, SMZ = Substrate Mixed Zone.

3.4. Thermal Profiles during SLM

Fig. 7 shows the (top) two-dimensional and (bottom) centreline temperature profiles on the powder surface during SLM as acquired by the IR camera as the laser beam moved from right to left. A moving frame-of-reference was used due to the steady-state nature of the process and thus position $(x, y) = (0, 0)$ corresponds to the centre of the laser. The x-coordinate can additionally be converted to a time coordinate by dividing by the laser scanning speed. Negative horizontal coordinates represent positions in front of the laser or in the future for a spatial- and time-based coordinate, while positive horizontal coordinates represent the position behind the laser or in the past. Due to the 1273 K minimum temperature limit, the thermal profile was only generated between -1 and 1.5 mm, or -2.5 to 3.75 ms.

As can be seen in the figure, when the laser arrived, the powder heated rapidly at a rate of $\approx$ 3,000 K/ms (point i) to a temperature of 2830 K (point ii). This value is above the melting temperatures of the Ti, AlV, and Fe powders as well as the Ti-185 alloy. The powder then cooled rapidly at an initial rate of $\approx$ 2,000 K/ms (point iii), spending 1.5 ms molten before solidifying, and then cooling at a rate of $\approx$ 200 K/ms (point iv).

Fig. 8 a) shows the sub-surface temperatures estimated via the Rosenthal equation, while 8 b) shows the maximum temperature predicted along the build direction. For this calculation, α was set to 0.51 in order to match the calculated melt pool width with the measured value seen in Fig. 7. This value is in line with previ-

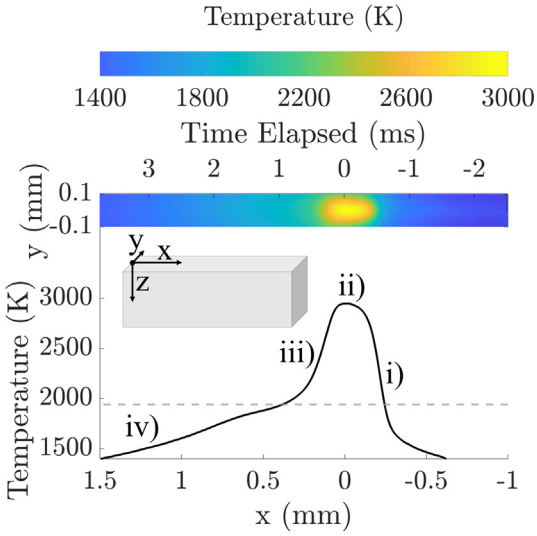

Fig. 7. Time- and position-dependent temperature profile at the surface as a (top) two-dimensional map and (bottom) one-dimensional centreline profiles during SLM. For reference, the melting point of titanium (1941 K) is also plotted as a gray, dotted line. At points i) and iii), the heating and cooling rates are 3,000 and 2,000 K/ms respectively; at point ii), the maximum temperature observed, 2830 K; at point iv), a cooling rate of $\approx$ 200 K/ms is observed. For reference, an image showing the coordinates on the sample is included in the top-left region of the bottom plot. To interpret the colour in this figure, please refer to the web version of this paper.).

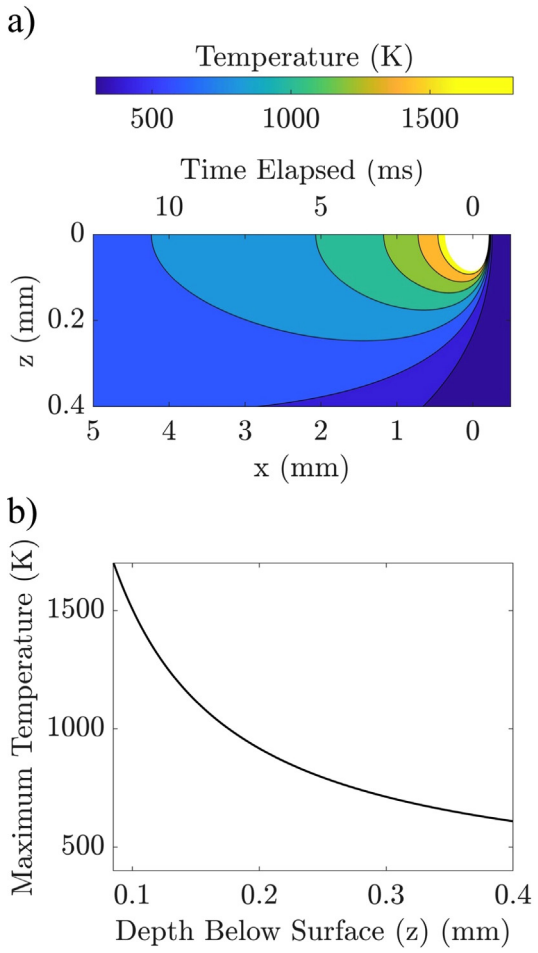

Fig. 8. a) Estimation of the steady-state sub-surface temperatures via the Rosenthal equation. b) Maximum temperature below the melt pool as a function of depth. Note that the *z* axis in a) is not to scale to emphasize this direction. To interpret the colour in this figure, please refer to the web version of this paper.

ous studies, which utilized α-values of 0.34–0.53 in the transition mode between conduction and keyholing modes [44]. As was shown in Section 3.3, melt pool shapes of this type were observed. The melt pool depth was $\sim$ 85 μm, indicating that at least 3–4 layers below the powder layer underwent remelting during each laser pass. This differed from the actual depth of $\sim$ 100 μm at the edge, and $\sim$ 140 μm at the centreline, as shown in Fig. 5. This demonstrates that factors not included in the Rosenthal equation itself were in play, including the exothermic mixing enthalpy of Ti-185 (-4.085 kJ/mol at 2500 K), a mixed keyholing-and-conduction-mode melt pool, and the heterogeneous nature of the powder. The β-transus of pure Ti (1155 K) was reached at depths of up to 145 μm, while the β-transus of Ti-185 (970.68 K) was reached at depths up to 185 μm.

4. Discussion

4.1. Completion of Homogeneity

By combining the sXRD plots in Figs. 3 and 4, the EDX maps in Fig. 5) and the EBSD phase maps in Figs. 6), a clear view of *in situ* alloying during SLM is presented. We define this as a three-step process: (1) partial alloying of elements in the melt pool; (2) continued elemental diffusion in the heat-affected zone; and (3) completion of alloying by the end of the heat-affected zone.

Step 1: In the melted zone, there exists a significant competition between the large heat imparted and the rapid heat diffusion that defines the solidified microstructure. On one hand, there were intense heat inputs: a laser power of 200 W narrowly focused to a spot size of 50 μm, and an exothermic mixing enthalpy (-4.085 kJ/mol at 2500 K). As a result, the temperature reached up $\approx$ 2800 K. On the other hand, the narrowly-focused heat dissipated rapidly. Thus the powder was molten for only 1.5 ms, while the subsequent solid state phase transformation took only 36 ± 14 ms (Figs. 3 and 4) which offered very little time for atomic diffusion. As a result, the powders only partially mixed during melting. This was demonstrated in Fig. 5 b), where the melt pool contained regions consistent in concentration, and regions high in one element but lower in the other elements. EBSD verified this finding by showing a mixture of β and martensitic α, i.e. α', in the melted zone. Martensitic laths occur in regions insufficiently β-stabilized when cooled at minimum rates of a few hundred K/s [45]. Thus, the α phase occurs in the regions high in Ti and Al, while the β phase is found in the regions low in Ti and Al.

Step 2: In the heat-affected-zone, mixing also depends on the competition between the heat imparted and heat dissipated. Here, the mixing enthalpy is also exothermic (-0.170 kJ/mol at 900 K). Maximum temperatures and cooling rates are lower than those in the melted zone. For example, the bottom of the heat-affected-zone, according to the Rosenthal solution, reached 835 K. The maximum cooling rate ranged between 75 K/ms at 140 μm to 17 K/ms at 230 μm. As a result of slower heat dissipation, further mixing occurs during each reheating cycle, as shown in the increasingly consistent microstructures from 140 to 230 μm in the EDX image, Fig. 5 b). This is verified by the EBSD phase map in Fig. 6 b) that shows an increasing β phase fraction (and decreasing α) with increasing depth below the top surface. Further mixing caused more α to be converted to β. Fig. 6 b) also shows α at β grain boundaries. The lower cooling rates induced the formation of grain boundary α, which only forms upon aging β-Ti (i.e. heating it below the β-transus) [45].

Step 3: Alloying is seen to be complete at the end of the heat-affected-zone. Within the alloyed zone, the heat imparted from the laser is negligible thus neither causing microstructural refinement nor significant atomic diffusion and hence. The consistent microstructure in this region with β-grains and sub-microscopic grain-boundary α and up to the substrate-mixed region (seen in both the elemental and phase maps in Figs. 7 b) and 8 b)) shows that alloying has been achieved.

4.2. Comparison with Other Works on SLM-printed Ti-185 and In Situ Alloying

The degree of mixing and the depth whereby mixing continues to occur during SLM depends greatly on the interplay between heat input and heat dissipation. Our previous work on printing Ti-185 from BE powder obtained a mixed α+β structure instead of mainly β with sub-microscopic grain-boundary α [28]. However that study used a lower energy density of 50.4 J/mm^3, rather than 66.7 J/mm^3 used in this work. Further, the larger dimensions of the sample in [28] enabled more heat dissipation and hence higher cooling rates, allowing retention of more β. Hence, less energy was imparted per layer and less α at the edge of the melt pool boundaries was converted to β. Although Azizi et al. showed homogeneity throughout the structure [28], the wall printed in this work only achieved homogeneity at the centreline, but not at the edges. This was likely due to the use of single-track SLM and not the hatching process applied when printing with an industrial SLM machine. Hatch spacing would facilitate homogenization away from the centre of the melt pool.

This work verifies what has previously been shown by Dobbelstein et al. [5] in that the surface of a laser-printed alloy is not homogenous. It expands on this by showing how mixing occurs through repeated passes of the laser. This work also confirms the observation of a graded structure between the top and bottom of a single wall laser-printed from BE powder by Yan et al. and Kang et al. [25,26]. It takes this work further by analysing the transformation from the melted zone to the bulk microstructure, via the heat-affected zone. This research has also used sXRD, in addition to conventional electron microscopy techniques, to explain the phase transformations in the microstructure, and relate them directly back the degree of alloying. Ultimately, this research has described how a single layer of BE powder undergoes multiple intrinsic heating cycles as it develops into a bulk, homogenous microstructure.

Finally, the results of this investigation show that contrary to many prior studies (of [23,5,46,14,47,18,22,19,24,48,49,7,13,50]), the presence of unmelted powders at the surface is not a useful metric for determining if exposed layers in a sample are alloyed. Even though sintered unmelted powders may be absent on exposed surfaces, the distribution of alloying elements will still be uneven, and not match the desired microscopic concentration. If one desires to preserve exposed layers in a structure, for example, a lattice or honeycomb structure, remelting each layer after building it (or a similar technique) could be performed. Past research [23,51,46,5,52,53] has shown that this technique produces few unmelted particles at the surface without a high laser power thus limiting defect including keyholing or excessive vaporization.

5. Conclusions

This study provided a clear picture of the process of *insitu* alloying from a BE powder mixture to an alloyed microstructure. Specifically, the three stage process of alloying during SLM has, for the first time, been observed. First, hindered by a rapid transformation time but aided by the high melt pool temperature and an exothermic mixing enthalpy, only partial alloying occurs in the melted zone, with mixed and unmixed regions randomly distributed within the former melt pool. Second, in the heat-affected zone, the process of elemental diffusion is accelerated by the laser heat and exothermic mixing. Third, towards the end of the heat-affected zone, complete alloying achieved. The insight on how *in situ* alloying occurs and the factors influencing it provided by this research can be employed to design optimal printing processes for alloys printed from BE powder.

Declaration of Competing Interest

The authors declare that they have no known competing financial interests or personal relationships that could have appeared to influence the work reported in this paper.

Acknowledgements

FA, NH, HZ, and ABP acknowledge the funding provided by the Natural Sciences and Engineering Council of Canada, the Ontario Centre for Innovation, and Collins Aerospace in support of this research. SC, CLAL, SM, and PDL acknowledge funding provided by MAPP: EPSRC Future Manufacturing Hub in Manufacture using Advanced Powder Processes (EP/P006566/1), EPSRC Impact Acceleration (EP/R511638/1), as well as a Royal Academy of Engineering Chair in Emerging Technology (CiET1819/10) and the Office of Naval Research (ONR) Grant N62909-19-1–2109. We thank the European Synchrotron Radiation Facility for access to Beamline ID31 (MA 3971), L. Sinclair and Y. Chen who helped with the beamtime, the Canadian Centre for Electron Microscopy for access to its SEMs and expertise, Dr. Khaled Abu Samk for running ThermoCalc, Dr. Mirnaly Saenz de Miera for operating EBSD, Dr. Jim Britten and Victoria Jarvis at the McMaster Analytical X-ray Diffraction Facility for fruitful discussion, and Dr. Samy Hocine for his feedback.

Appendix A. Supplementary material

Supplementary data associated with this article can be found, in the online version, at https://doi.org/10.1016/j.matdes.2021.110072.

References

[1] W.J. Sames, F.A. List, S. Pannala, R.R. Dehoff, S.S. Babu, The metallurgy and processing science of metal additive manufacturing, Int. Mater. Rev. 61 (5) (2016) 315–360, https://doi.org/10.1080/09506608.2015.1116649.
[2] D.D. Gu, W. Meiners, K. Wissenbach, R. Poprawe, Laser additive manufacturing of metallic components: Materials, processes and mechanisms, Int. Mater. Rev. 57 (3) (2012) 133–164, https://doi.org/10.1179/1743280411Y.0000000014.
[3] P.A. Hooper, Melt pool temperature and cooling rates in laser powder bed fusion, Additive Manufacturing 22 (2018) 548–559, https://doi.org/10.1016/j.addma.2018.05.032.
[4] D. Bourell, J.P. Kruth, M. Leu, G. Levy, D. Rosen, A.M. Beese, A. Clare, Materials for additive manufacturing, CIRP Annals - Manufacturing Technology 66 (2017) 659–681, https://doi.org/10.1016/j.cirp.2017.05.009.
[5] H. Dobbelstein, M. Thiele, E.L. Gurevich, E.P. George, A. Ostendorf, Direct metal deposition of refractory high entropy alloy MoNbTaW, Physics Procedia 83 (2016) 624–633, https://doi.org/10.1016/j.phpro.2016.08.065.
[6] T. Nagase, T. Hori, M. Todai, S.-H. Sun, T. Nakano, Additive manufacturing of dense components in beta-titanium alloys with crystallographic texture from a mixture of pure metallic element powders, Mater. Des. 173 (2019) 107771, https://doi.org/10.1016/j.matdes.2019.107771.
[7] V. Fallah, S.F. Corbin, A. Khajepour, Process optimization of Ti-Nb alloy coatings on a Ti-6Al-4V plate using a fiber laser and blended elemental powders, J. Mater. Process. Technol. 210 (2010) 2081–2087, https://doi.org/10.1016/j.jmatprotec.2010.07.030.
[8] S. Ewald, F. Kies, S. Hermsen, M. Voshage, C. Haase, J.H. Schleifenbaum, Rapid alloy development of extremely high-alloyed metals using powder blends in laser powder bed fusion, Materials 12 (10) (2019) 1706, https://doi.org/10.3390/MA12101706.
[9] I. Polozov, V. Sufiiarov, A. Popovich, D. Masaylo, A. Grigoriev, Synthesis of Ti-5Al, Ti-6Al-7Nb, and Ti-22Al-25Nb alloys from elemental powders using powder-bed fusion additive manufacturing, J. Alloy. Compd. 763 (2018) 436–445, https://doi.org/10.1016/j.jallcom.2018.05.325.
[10] T. Hanemann, L.N. Carter, M. Habschied, N.J. Adkins, M.M. Attallah, M. Heilmaier, In-situ alloying of AlSi10Mg+Si using Selective Laser Melting to control the coefficient of thermal expansion, J. Alloy. Compd. 795 (2019) 8–18, https://doi.org/10.1016/j.jallcom.2019.04.260.
[11] R. Martinez, I. Todd, K. Mumtaz, In situ alloying of elemental Al-Cu12 feedstock using selective laser melting, Virtual and Physical Prototyping 14 (3) (2019) 242–252, https://doi.org/10.1080/17452759.2019.1584402.
[12] H. Schönrath, M. Spasova, S.O. Kilian, R. Meckenstock, G. Witt, J.T. Sehrt, M. Farle, Additive manufacturing of soft magnetic permalloy from Fe and Ni powders: Control of magnetic anisotropy, J. Magn. Magn. Mater. 478 (2019) 274–278, https://doi.org/10.1016/j.jmmm.2018.11.084.
[13] D. Zhao, C. Han, Y. Li, J. Li, K. Zhou, Q. Wei, J. Liu, Y. Shi, Improvement on mechanical properties and corrosion resistance of titanium-tantalum alloys in-situ fabricated via selective laser melting, J. Alloy. Compd. 804 (2019) 288–298, https://doi.org/10.1016/j.jallcom.2019.06.307.
[14] K.D. Traxel, A. Bandyopadhyay, Reactive-deposition-based additive manufacturing of Ti-Zr-BN composites, Additive Manufacturing 24 (2018) 353–363, https://doi.org/10.1016/j.addma.2018.10.005.
[15] S.L. Sing, F.E. Wiria, W.Y. Yeong, Selective laser melting of titanium alloy with 50 wt% tantalum: Effect of laser process parameters on part quality, Int. J. Refract. Met. Hard Mater. 77 (2018) 120–127, https://doi.org/10.1016/j.ijrmhm.2018.08.006.
[16] J.C. Wang, Y.J. Liu, P. Qin, S.X. Liang, T.B. Sercombe, L.C. Zhang, Selective laser melting of Ti–35Nb composite from elemental powder mixture: Microstructure, mechanical behavior and corrosion behavior, Mater. Sci. Eng., A 760 (2019) 214–224, https://doi.org/10.1016/j.msea.2019.06.001.
[17] C.A. Biffi, A.G. Demir, M. Coduri, B. Previtali, A. Tuissi, Laves phases in selective laser melted TiCr1.78 alloys for hydrogen storage, Mater. Lett. 226 (2018) 71–74, https://doi.org/10.1016/j.matlet.2018.05.028.
[18] I. Polozov, V. Sufiiarov, A. Kantyukov, A. Popovich, Selective Laser Melting of Ti2AlNb-based intermetallic alloy using elemental powders: Effect of process parameters and post-treatment on microstructure, composition, and properties, Intermetallics 112 (2019) 106554.
[19] H. Chen, X. Zi, Y. Han, J. Dong, S. Liu, C. Chen, Microstructure and mechanical properties of additive manufactured W-Ni-Fe-Co composite produced by

selective laser melting, Int. J. Refract. Met. Hard Mater. 86 (2020) 105111, https://doi.org/10.1016/j.ijrmhm.2019.105111.
[20] M. Tlotleng, B. Masina, S. Pityana, Characteristics of Laser In-situ Alloyed Titanium Aluminides Coatings, Procedia Manufacturing 7 (2017) 39–45, https://doi.org/10.1016/j.promfg.2016.12.013.
[21] C. Wang, X.P. Tan, Z. Du, S. Chandra, Z. Sun, C.W.J. Lim, S.B. Tor, C.S. Lim, C.H. Wong, Additive manufacturing of NiTi shape memory alloys using pre-mixed powders, J. Mater. Process. Technol. 271 (2019) 152–161.
[22] P. Chen, S. Li, Y. Zhou, M. Yan, M.M. Attallah, Fabricating CoCrFeMnNi high entropy alloy via selective laser melting in-situ alloying, J. Mater. Sci. Technol. 43 (2020) 40–43, https://doi.org/10.1016/j.jmst.2020.01.002.
[23] M. Moorehead, K. Bertsch, M. Niezgoda, C. Parkin, M. Elbakhshwan, K. Sridharan, C. Zhang, D. Thoma, A. Couet, High-throughput synthesis of Mo-Nb-Ta-W high-entropy alloys via additive manufacturing, Mater. Des. 187 (2020) 108358, https://doi.org/10.1016/j.matdes.2019.108358.
[24] K. Geng, Y. Yang, S. Li, R.D. Misra, Q. Zhu, Enabling high-performance 3D printing of Al powder by decorating with high laser absorbing Co phase, Additive Manufacturing 32 (2020) 101012, https://doi.org/10.1016/j.addma.2019.101012.
[25] L. Yan, X. Chen, W. Li, J. Newkirk, F. Liou, Direct laser deposition of Ti-6Al-4V from elemental powder blends, Rapid Prototyping Journal 22 (5) (2016) 810–816.
[26] N. Kang, X. Lin, M.E. Mansori, Q.Z. Wang, J.L. Lu, C. Coddet, W.D. Huang, On the effect of the thermal cycle during the directed energy deposition application to the in-situ production of a Ti-Mo alloy functionally graded structure, Additive Manufacturing 31 (2020) 100911, https://doi.org/10.1016/j.addma.2019.100911.
[27] C. Leyens, M. Peters (Eds.), Titanium and Titanium Alloys: Fundamentals and Applications, Wiley-VCH Verlag GmbH & Co. KGaA, Weinheim, 2003.
[28] H. Azizi, H. Zurob, B. Bose, S.R. Ghiaasiaan, X. Wang, S. Coulson, V. Duz, A.B. Phillion, Additive manufacturing of a novel Ti-Al-V-Fe alloy using selective laser melting, Additive Manufacturing 21 (2018) 529–535, https://doi.org/10.1016/j.addma.2018.04.006.
[29] N.P. Calta, J. Wang, A.M. Kiss, A.A. Martin, P.J. Depond, G.M. Guss, V. Thampy, A. Y. Fong, J. Nelson Weker, K.H. Stone, C.J. Tassone, M.J. Kramer, M.F. Toney, A. Van Buuren, M.J. Matthews, An instrument for in situ time-resolved X-ray imaging and diffraction of laser powder bed fusion additive manufacturing processes, Rev. Sci. Instrum. 89 (2018) 055101, https://doi.org/10.1063/1.5017236.
[30] N.P. Calta, V. Thampy, D.R. Lee, A.A. Martin, R. Ganeriwala, J. Wang, P.J. Depond, T.T. Roehling, A.Y. Fong, A.M. Kiss, C.J. Tassone, K.H. Stone, J. Nelson Weker, M. F. Toney, A.W. Van Buuren, M.J. Matthews, Cooling dynamics of two titanium alloys during laser powder bed fusion probed with in situ X-ray imaging and diffraction, Mater. Des. 195 (2020) 108987, https://doi.org/10.1016/j.matdes.2020.108987.
[31] J. Epp, J. Dong, H. Meyer, A. Bohlen, Analysis of cyclic phase transformations during additive manufacturing of hardenable tool steel by in-situ X-ray diffraction experiments, Scripta Mater. 177 (2020) 27–31, https://doi.org/10.1016/j.scriptamat.2019.09.021.
[32] S. Hocine, S. Van Petegem, U. Frommherz, G. Tinti, N. Casati, D. Grolimund, H. Van Swygenhoven, A miniaturized selective laser melting device for operando X-ray diffraction studies, Additive Manufacturing 34 (2020) 101194, https://doi.org/10.1016/j.addma.2020.101194.
[33] S. Hocine, H. Van Swygenhoven, S. Van Petegem, C.S.T. Chang, T. Maimaitiyili, G. Tinti, D. Ferreira Sanchez, D. Grolimund, N. Casati, Operando X-ray diffraction during laser 3D printing, Mater. Today 34 (2020) 30–40, https://doi.org/10.1016/j.mattod.2019.10.001.
[34] F. Schmeiser, E. Krohmer, N. Schell, E. Uhlmann, W. Reimers, Experimental observation of stress formation during selective laser melting using in situ X-ray diffraction, Additive Manufacturing 32 (2020) 101028, https://doi.org/10.1016/j.addma.2019.101028.
[35] H. Okamoto, Al-V (Aluminum-Vanadium), Journal of Phase Equilibria and Diffusion 22 (1) (2001) 86, https://doi.org/10.1361/105497101770339355.
[36] C.L.A. Leung, S. Marussi, R.C. Atwood, M. Towrie, P.J. Withers, P.D. Lee, In situ X-ray imaging of defect and molten pool dynamics in laser additive manufacturing, Nature Communications 9 (2018) 1355, https://doi.org/10.1038/s41467-018-03734-7.
[37] C.L.A. Leung, S. Marussi, M. Towrie, R.C. Atwood, P.J. Withers, P.D. Lee, The effect of powder oxidation on defect formation in laser additive manufacturing, Acta Mater. 166 (2019) 294–305, https://doi.org/10.1016/j.actamat.2018.12.027.
[38] Y. Chen, S.J. Clark, C.L.A. Leung, L. Sinclair, S. Marussi, M.P. Olbinado, E. Boller, A. Rack, I. Todd, P.D. Lee, In-situ Synchrotron imaging of keyhole mode multi-layer laser powder bed fusion additive manufacturing, Applied Materials Today 20 (2020) 100650, https://doi.org/10.1016/j.apmt.2020.100650.
[39] L. Sinclair, C.L.A. Leung, S. Marussi, S.J. Clark, Y. Chen, M.P. Olbinado, A. Rack, J. Gardy, G. Baxter, P.D. Lee, In situ radiographic and ex situ tomographic analysis of pore interactions during multilayer builds in laser powder bed fusion, Additive Manufacturing (2020) 101512. doi:https://doi.org/10.1016/j.addma.2020.101512.
[40] Z.Y. Liu, C. Li, X.Y. Fang, Y.B. Guo, Energy Consumption in Additive Manufacturing of Metal Parts, Procedia Manufacturing 26 (2018) 834–845, https://doi.org/10.1016/j.promfg.2018.07.104. URL http://www.sciencedirect.com/science/article/pii/S2351978918307753.
[41] V. Honkimäki, A Matlab package for the analysis of diffraction patterns collected using CdTe detectors, personal communication.
[42] S. Bontha, N.W. Klingbeil, P.A. Kobryn, H.L. Fraser, Thermal process maps for predicting solidification microstructure in laser fabrication of thin-wall structures, J. Mater. Process. Technol. 178 (1–3) (2006) 135–142, https://doi.org/10.1016/j.jmatprotec.2006.03.155.
[43] D. Rosenthal, The theory of moving sources of heat and its applications to metal treatments, Transactions of the ASME 68 (8) (1946) 849–866.
[44] T.R. Allen, W. Huang, J.R. Tanner, W. Tan, J.M. Fraser, B.J. Simonds, Energy-Coupling Mechanisms Revealed through Simultaneous Keyhole Depth and Absorptance Measurements during Laser-Metal Processing, Physical Review Applied 13 (2020) 06070, https://doi.org/10.1103/PhysRevApplied.13.064070.
[45] S. Banerjee, P. Mukhopadyay, Phase Transformations: Examples from Titanium and Zirconium Alloys, Pergamon, Oxford, 2007.
[46] H. Dobbelstein, E.L. Gurevich, E.P. George, A. Ostendorf, G. Laplanche, Laser metal deposition of compositionally graded TiZrNbTa refractory high-entropy alloys using elemental powder blends, Additive Manufacturing 25 (2019) 252–262, https://doi.org/10.1016/j.addma.2018.10.042.
[47] H. Attar, M. Bönisch, M. Calin, L.C. Zhang, K. Zhuravleva, A. Funk, S. Scudino, C. Yang, J. Eckert, Comparative study of microstructures and mechanical properties of in situ Ti-TiB composites produced by selective laser melting, powder metallurgy, and casting technologies, J. Mater. Res. 29 (17) (2014) 1941–1950, https://doi.org/10.1557/jmr.2014.122.
[48] C. Haase, F. Tang, M.B. Wilms, A. Weisheit, B. Hallstedt, Combining thermodynamic modeling and 3D printing of elemental powder blends for high-throughput investigation of high-entropy alloys – Towards rapid alloy screening and design, Mater. Sci. Eng., A 688 (January) (2017) 180–189, https://doi.org/10.1016/j.msea.2017.01.099.
[49] K.I. Schwendner, R. Banerjee, P.C. Collins, C.A. Brice, H.L. Fraser, Direct laser deposition of alloys from elemental powder blends, Scripta Mater. 45 (2001) 1123–1129.
[50] D. Zhao, C. Han, J. Li, J. Liu, Q. Wei, In situ fabrication of a titanium-niobium alloy with tailored microstructures, enhanced mechanical properties and biocompatibility by using selective laser melting, Mater. Sci. Eng., C 111 (2020) 110784.
[51] H. Dobbelstein, E.L. Gurevich, E.P. George, A. Ostendorf, G. Laplanche, Laser metal deposition of a refractory TiZrNbHfTa high-entropy alloy, Additive Manufacturing 24 (2018) 386–390.
[52] E.G. Brodie, A.E. Medvedev, J.E. Frith, M.S. Dargusch, H.L. Fraser, A. Molotnikov, Remelt processing and microstructure of selective laser melted Ti25Ta, J. Alloy. Compd. 820 (2020) 153082, https://doi.org/10.1016/j.jallcom.2019.153082.
[53] D. Lin, L. Xu, X. Li, H. Jing, G. Qin, H. Pang, F. Minami, A Si-containing FeCoCrNi high-entropy alloy with high strength and ductility synthesized in situ via selective laser melting, Additive Manufacturing 35 (2020) 101340, https://doi.org/10.1016/j.addma.2020.101340.